Aeroelastic Wing Performance in High Intensity Free-stream Turbulence: Integral Length Scale Effects

Craig Thompson *, Hulya Biler†, Sean Symon‡, and Bharathram Ganapathisubramani§
University of Southampton, Burgess Rd, Southampton SO16 7QF, UK

The impact of variations in the integral length scale of incoming free-stream turbulence on an aeroelastic NACA0012 wing is investigated using force, moment and PIV measurements. At a chord-based Reynolds number ($Re = U_\infty c/\nu$) of $2 \cdot 10^5$, an active grid generates turbulence intensities of 15 % at normalised integral length scales ranging from $0.5c$ to $1c$ (c is the chord length). The introduction of turbulence improves the time-averaged performance characteristics of the aeroelastic wing by delaying stall and increasing the peak lift coefficient. The turbulence excites structural modes such as bending and torsion but it does not introduce new frequencies in the forces and moments. Instead, it amplifies particular frequencies that appear in the clean flow case. It is observed that for full-chord integral length scales, the magnitude of the fluctuations in forces and moments at the frequency of a structural bending mode is excited. Meanwhile, at half-chord integral length scales, the magnitude of the fluctuations in forces and moments at the frequency of a torsional response is excited. The structural excitations resulting from the incoming turbulence in turn generate unique characteristics in the flow field surrounding the aeroelastic wing.

I. Introduction

The wings of birds have been a source of inspiration for the design of aircraft for decades, with the introduction of mechanisms such as split scimitar winglets, sweep, or flexibility. In particular, the flexibility of a bird's wing is a key factor that enables safe flight in turbulent conditions within the atmospheric boundary layer, utilising passive gust mitigation effects [1]. Micro air vehicles (MAVs) also operate within the atmospheric boundary layer, especially in urban environments where the turbulence intensities are typically 10-20 % at length scales of up to 10 times the order of magnitude of the aircraft's chord [2]. To mitigate the effects of the high intensity turbulence, aeroelastic wings are often fitted to MAVs. The study of aeroelasticity in MAVs is particularly challenging due to their small size and low Reynolds number flight regime. Moreover, it is known that the complex interaction between the aeroelasticity of the wing, and the turbulent inflow can cause structural excitations. Therefore, by analyzing the behavior of aeroelastic

*PhD Candidate, Department of Aeronautics and Astronautics, University of Southampton, ct4g16@soton.ac.uk.
†Research Associate, Department of Aeronautics and Astronautics, University of Southampton.
‡Associate Professor, Department of Aeronautics and Astronautics, University of Southampton.
§Professor of Experimental Fluid Mechanics, Department of Aeronautics and Astronautics, University of Southampton.

wings in free-stream turbulence (FST), we aim to gain insights into the development of these structural excitations and hence provide important understanding into the design of MAVs operating in turbulent conditions.

There exists a rich body of literature exploring deformable lifting surfaces in steady flows at low Reynolds numbers, resulting from the increased demand of MAVs [3, 4]. It is found that the addition of flexibility to the wings of MAV's improves many flight characteristics such as an improvement to the stability within gusty environments resulting from changes in apparent angle of attack. Gursul et al. [5] find different structural modes are excited due to the flow separation in a steady free-stream. These self-excited surface oscillations (of a membrane wing or a slightly flexible wing) induce leading-edge vortices, resulting in a lift increase and drag reduction. Additionally, work by Qinfeng et al. [6] found a flexible membrane wing can delay the onset of stall by 5-degrees and increase the lift by 90 % when compared to a rigid wing. The reasoning behind these improved characteristics corresponds to a larger deformation and stronger vibration of the wing. This leads to stronger flow mixing near the flexible wing surface, which suppresses leading-edge separation and therefore significantly improves the aerodynamic performance.

One of the first investigations into the response of an aeroelastic aerodynamic surface to flow perturbations is by Tang et al. [7]. In this study, a rotor blade is subjected to periodic gusts generated by a rotating slotted cylinder [8], capable of producing controllable single or multiple harmonic lateral gusts. It is observed that once stall occurs, the nonlinearity of both the structure and aerodynamics is significant. Moreover, at large angles of attack the twist response is aperiodic whereas the bending response is seen to be periodic. This study, alongside similar work, found that the structural natural frequencies of wings are excited by both single and multiple harmonic gusts, for a variety of wing structures and gust strengths [9–11].

The unsteady nature of the fluid-structure interaction of aeroelastic wings is investigated by Tang and Dowell [12]. Employing a large aspect ratio aeroelastic wing with a tip mass, the study explored static aeroelastic response, flutter, and limit cycle oscillations. The investigation observed beam-like structural behaviour and found that the onset of a limit cycle oscillation is dominated by stall aerodynamics. A comprehensive overview of current aeroelastic knowledge, with a specific emphasis on limit cycle oscillations, is presented by Dowell [13]. This work underscores the critical role of external disturbances, such as FST, in the development of dynamic nonlinearities—a focal point of the present research.

In a recent investigation by Fernandez et al. [14], the lift, flow field, and deformation of two aeroelastic wings and one rigid wing are measured under periodic gusts. The gusts are generated by a novel irrotational method, termed an oscillating fence [15]. Each wing has a NACA0012 profile and is positioned at angles of attack of 0 to 12 degrees for $Re = 3.15 \cdot 10^5$. The low flexibility wing has a bending frequency of 3.42 Hz and the high flexibility wing has a bending frequency of 1.9 Hz, chosen to coincide with the frequency of the periodic gusts generated. It is observed that if the gust frequency is similar to the natural frequency of the bending mode of the aeroelastic wing, the gust excites that mode. This result suggests that if the unsteady nature of the incoming flow is correctly tailored to the airfoil's geometry, significant structural modes within geometry are amplified by the flow disturbances.

Initial exploration into the effect of FST on airfoil characteristics was conducted by Hoffmann [16]. The study revealed that, at the highest FST level (9 %), there is a 30 % increase in the peak lift coefficient, accompanied by a 5-degree delay in the onset of stall. Work by Refs. [17–19] found a 64 % increase in lift is achieved for a wing submerged in the turbulent wake of a bluff body with the correct wake distance and geometry. A review of similar investigations on the influence of FST on rigid wings is presented within Thompson et al. [20] where there is a notable gap in research regarding aeroelastic wings subjected to FST.

It is discussed in previous literature that harmonic flow perturbations can cause amplifications of the structural modes of an aeroelastic wing, particularly for angles where the wing is stalled. However, the effects of FST on aeroelastic wings are unexplored. Therefore the aim of this paper is to investigate the effect of high intensity FST at various integral length scales on the response of an aeroelastic wing. The work herein will determine if structural amplifications can be excited by exploring the effects of the integral length scale of FST on the performance of an aeroelastic wing, both in pre- and post-stall conditions. We focus on high FST ($\approx$15 %) and vary the integral length scale of the turbulence from $0.5c$ to $1c$. Particular attention is paid to understanding the changes in force and moment fluctuations of the response of an aeroelastic wing, along with an examination of how the surrounding flow field both induces and responds to these fluctuations.

In the following sections, we present results from experimental campaigns and subsequent analysis of the data of an aeroelastic wing subjected to FST. Section II outlines the experimental methodology, section III discusses the results obtained from the experimental campaigns, and implements several numerical techniques to interpret those measurements. Finally, section IV concludes our findings.

II. Experimental methods

A. Wing model

The aeroelastic rectangular wing has a finite-aspect ratio of 2.5 with a NACA0012 profile, featuring a 0.75 m span and 0.3 m chord, with no flow tripping devices applied to the wing's surface. As seen in figure 1, the wing is constructed with a 3 mm aluminum sheet sandwiched between two pieces of high density foam. This design gives it flexibility while ensuring essential structural strength.

Fig. 1 Cross section of the aeroelastic NACA 0012 wing, where black represents foam and grey represents a 3 mm thick aluminum plate.

Assuming that the wing's structural response can be modeled using the aluminum plate, beam theory can be applied

to determine the structural properties. The density of the wing is 2700 kgm^{-3}. The flexural and torsional stiffness are calculated as $3EI/L^3$ and GJ/L, respectively [21], where E represents a Young's modulus of 69 GPa, I represents a moment of inertia of $6.75 \cdot 10^{-10}$ m^4, L represents a beam length of 0.75 m, G represents a shear modulus of 25.94 GPa, and J represents a polar moment of inertia of $1.24 \cdot 10^{-6}$ m^4. Therefore, the aeroelastic wing has a flexural stiffness of 331.3 Nm^{-1} and a torsional stiffness of $4.27 \cdot 10^4$ Nmrad^{-1}.

B. Digital image correlation

Digital image correlation (DIC) is a technique that measures the deformation and motion of an object by tracking the position of reflective tracer spots on its surface. It helps to characterise the structural modes of the aeroelastic wing system, such as bending, torsion, and surging, by analysing the displacement of the wing in different directions.

The wing is placed in the University of Southampton's 7 x 5 wind tunnel at a Reynolds number range of $Re = 3 \cdot 10^5 - 5 \cdot 10^5$. For the DIC experiments the angle of attack is fixed at 18-degrees post-stall. Figure 2 is for demonstration purposes, when conducting the measurements the wing is moved towards the center of the tunnel so the LED arrays do not cause any additional aerodynamic effects. Motion tracking tracer spots are placed on the aeroelastic wing with a nominal spacing of $1/6c$. Five Phantom v641 high-speed cameras are arranged outside the test section, alongside blue LED light arrays that highlight the tracer spots. A "shake the box" method is used to track the position of the tracer spots [22]. For the experiment, 5,450 sets of points in time are generated at a sampling rate of 200 Hz (equivalent to 1350 - 2250 convection cycles). Using a 6-axis ATI IP 65SI660 load cell, simultaneous measurements of forces and moments are measured during the DIC experiment. More information regarding forces and moments can be found in section II.D.

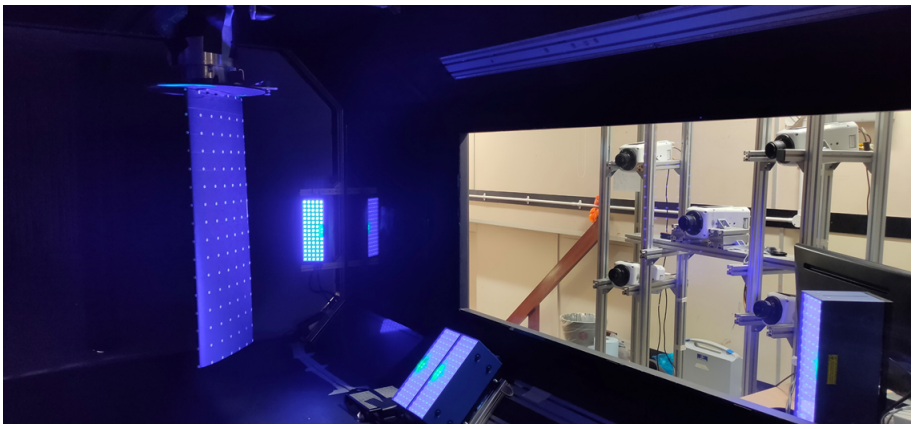

Fig. 2 DIC setup of the aeroelastic wing in the University of Southampton's 7 x 5 wind tunnel. This figure is for demonstration purposes only.

C. Turbulence generation

To understand how the integral length scale of FST affects a wing, the turbulence characteristics of the producible FST must be determined. All turbulent experiments are conducted within the University of Southampton's "Gottingen" type closed wind tunnel with a closed test section where the free-stream has a turbulence intensity of less than 0.1 % in clean configuration. A Makita style active grid with a grid spacing of M = 0.085 m is used to generate the FST. The grid produces homogeneous turbulence in the spanwise and cross-stream direction for all cases, with variations of less than ±2.5 % for the mean flow and turbulence statistics. Figure 3 shows the turbulence spectra, with a constant value in the production range and a $-5/3$ power law in the inertial range. Table 1 summarizes the turbulence intensity T_u and chord normalised integral length scale L_x/c of the FST as measured using hot wire anemometry (HWA).

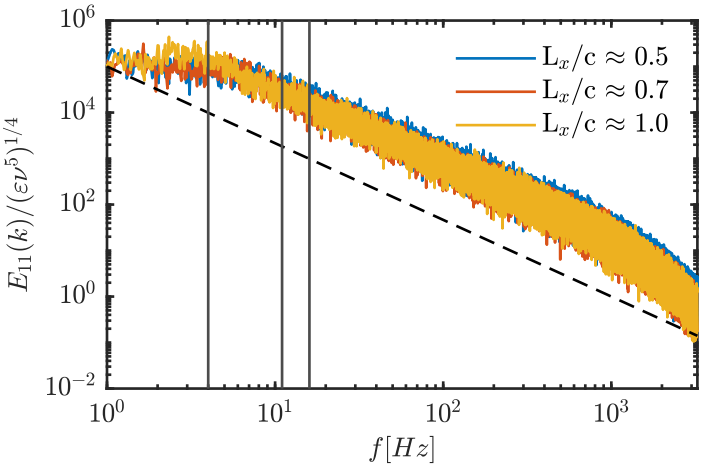

Fig. 3 Spectral content of turbulent cases from HWA. The angled dashed line represents Kolmogorov's -5/3 law. $Re = 2 \cdot 10^5$**.**

The turbulence intensity is determined as $T_u = U_{rms}/U_{mean}$ where U_{rms} is the root mean square of the velocity and U_{mean} is the mean velocity. The integral length scale is determined via the integration of the zero-crossing point of the autocorrelation, as shown in Equation (1) below:

$$L_x = U_\infty T_l, \tag{1}$$

$$T_l = \int_0^{T_{cross}} \rho_x(\tau)\, dt, \tag{2}$$

where τ is the time lag, T_{cross} is the zero crossing time and ρ_x is the auto correlation coefficient defined as:

$$\rho_x(\tau) = \frac{R_x(\tau)}{R_x(0)}, \tag{3}$$

where R_x is the auto correlation function in time.

The active grid's upper and lower limits of integral length scale are $L_{x,max} = 1.0c$, $L_{x,min} = 0.5c$ at a turbulence intensity of $T_u = 15\%$ for a maximum Reynolds number of $Re = 2 \cdot 10^5$. The limits of the active grid's turbulence characteristics are representative of turbulent flow conditions encountered in practical aerospace applications, particularly for micro air vehicles operating in urban environments. More information about the turbulence generation can be found in Thompson et al. [20].

Table 1 Turbulence characteristics.

T_u [%]	L_x/c
< 0.1	Clean
14.7	0.5
14.3	0.7
15.5	1.0

D. Forces and moments

Force and moment measurements are used to understand the aerodynamic performance and stability of an aeroelastic wing subjected to FST. By measuring the lift, drag, pitching moment, and bending moment at various angles of attack, the wing's response to different FST can be evaluated. The fluctuations in the forces and moments indicate the excitation of structural modes of the wing, such as bending, torsion and surging.

The wing is mounted to the ceiling of the tunnel test section such that the quarter chord is 1.8 m (21M) downstream of the active grid, which is chosen to ensure the wing experiences high intensity turbulence. Even though the distance to the grid is closer than the more commonly used 40M, volumetric hot wire analysis confirms that the grid produces homogeneous turbulence in the spanwise and cross-stream direction at this distance. A stepper motor is connected to the root of the wing allowing for a 360 degree range of motion. A 6-axis ATI IP65 SI165 load cell is placed at the root of the stepper motor to determine the forces and moments exerted by the wing. The measurement uncertainty at a 95 % confidence level as a percent of full-scale load is 1.25 %. With the system attached to the load cell, the resonance frequency of the ATI sensor drops to 90 Hz, over three times greater than the frequencies observed in this investigation. Figure 4 shows the PIV setup. The green areas represent the laser sheets, the blue and orange dashed lines indicate the field of view for each camera, and the grey cylinder represents the stepper motor and load cell. These devices extend outside the test section through transparent acrylic, ensuring that no additional aerodynamic effects are introduced by any part of the system. The root of the wing has a 2 mm clearance to the tunnel ceiling. A flow splitter is not implemented as a flexible wing is inherently three-dimensional. As such, the tunnel floor is a chord length from the wing tip. For all cases, the angle of attack is stepped from 0 to 20 degrees in increments of 1 degree. Following a sampling and convergence study, data is acquired at 1 kHz for 120 s (equivalent to 4000 convection cycles) at each angle. As a result of the three-dimensional nature of the wing, and the location of the load cell, the forces observed are integrated

across the wingspan and therefore the statistics that are measured by the load cell are filtered by the wing itself.

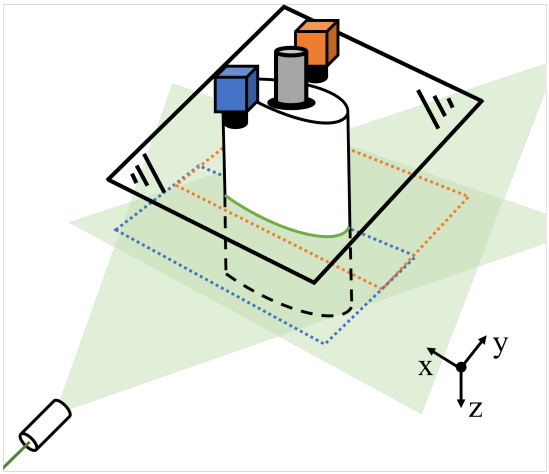

Fig. 4 Schematic representation of the PIV setup.

For each experimental campaign concurrent force and moment measurements are taken. In the DIC experiment, forces and moments are measured to simultaneously evaluate the deformation of the wing and the experienced forces. Similarly, in the PIV experiment, a channel of the data acquisition system used to measure the forces and moments from the load cell is connected to the laser trigger. This connection allows the timings of the acquired images to be concurrently matched to the resulting forces and moments produced by the wing. The forces and moments are sampled at a higher frequency of 10 kHz for the duration of the PIV case to ensure that each image trigger is captured. Table 2 shows the load cell and provides details about the sampling rate and the number of measurements chosen for each experimental campaign. The load cell was recalibrated for the lower Reynolds number experiments to increase the resolution in measuring smaller forces and moments.

Table 2 Load cell and sample information for DIC, force and moment, and PIV experimental campaigns

Experiment	Load cell	Sample rate [kHz]	Convection cycles 10^3
DIC	ATI IP65 SI660	10	3 - 5
Forces and moments	ATI IP65 SI165	1	4
PIV	ATI IP65 SI165	10	84

E. Particle image velocimetry

PIV is a technique for measuring the velocity field of a fluid flow and is used to investigate the flow field surrounding the aeroelastic wing in different turbulence conditions. PIV facilitates a deeper understanding of both the aerodynamics and structural response of the wing by allowing the identification and behaviour of coherent structures within the flow

field to be realised. The wing is mounted to the ceiling of the "Gottingen" type closed wind tunnel. Figure 4 shows the planar PIV set-up used to investigate the flow field surrounding the NACA0012 wing in the four aforementioned turbulence conditions at an angle of attack of 16 degrees at $Re = 2 \cdot 10^5$.

The PIV achieves a field of view of 475 mm × 800 mm surrounding the airfoil resulting in a resolution of 9.9 pixels per millimetre. The trade off to ensure a large field of view capable of capturing the wing's wake comes at the expense of resolving the boundary layer. Work by Istvan and Yarusevych [23] and Yarusevych and Kotsonis [24] concluded that a bypass transition effectively eliminates the laminar separation bubble at high turbulence intensities. Therefore, it is beneficial to explore an extended field of view that has not been previously measured. For each turbulence case 3,000 image pairs are captured at 0.6 Hz, and for each clean case 1,000 image pairs are captured at 0.6 Hz. More details about the PIV setup and post-processing methods can be found in Thompson et al. [20].

III. Results

A. Digital image correlation

Spectral proper orthogonal decomposition (SPOD), spectral analysis and surface fitting are used to characterise the structural modes of the aeroelastic wing system for angles post stall with a clean inflow.

The DIC data are divided into blocks containing 546 snapshots with 50 % overlap, resulting in 20 realizations of the flow. SPOD is performed using a Hamming window and further details of the algorithm can be found in Appendix IV.B. Figure 5 shows the chord normalised modal energy of the first 20 modes. Distinct peaks at 4 Hz, 11 Hz and 16 Hz are observed. The first mode of the peak at 4 Hz has an energy content an order of magnitude larger than that of the subsequent mode. Consequently, it captures nearly all the energy associated with the deformation at 4 Hz and dominates over the other modes. Figure 6 shows the first mode shape at 4 Hz for the streamwise (x) and cross-stream (y) direction. In the streamwise direction, the figure shows a solid color. Whereas, in the cross-stream direction, there is a clear gradient with a larger magnitude at the wing's tip that decreases towards the root, suggesting that a bending mode is present at this frequency.

When examining the modal energy associated with the 11 Hz peak, it becomes evident that the initial modes share comparable energy levels. In fact, the energy distribution across the first 10 modes falls within the same order of magnitude. Upon inspecting the mode shapes for these initial modes at 11 Hz, distinct torsional mode shapes emerge for each mode. Figure 6 shows the first mode shape at 11 Hz for the streamwise (x) and cross-stream (y) direction. A torsional mode is observed, however the presence of multiple modes with similar energy levels is attributed to the absence of a deterministic structure for torsion. Instead, all these modes occur at 11 Hz with comparable amplitudes which means that there is no preferred structure for this frequency. Consequently, relying on any single mode to determine structural information is inaccurate since many modes are energetic. Hence, a different approach is required

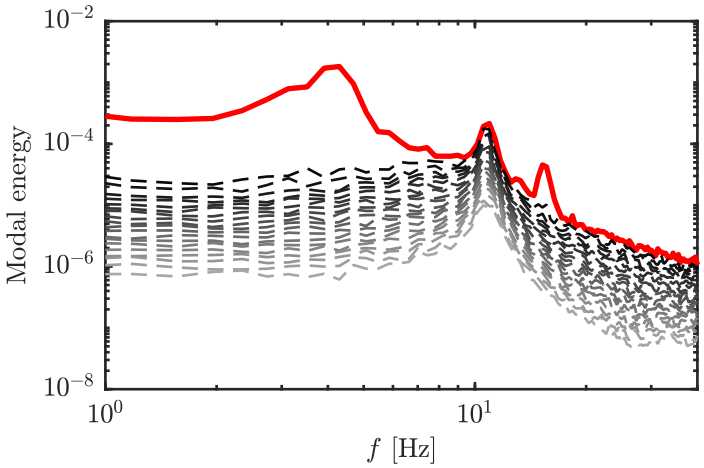

Fig. 5 Chord normalised modal energy of the (Red) first mode and (Grey) subsequent 19 modes. $\alpha = 18$ **degrees,** $Re = 5 \cdot 10^5$**.**

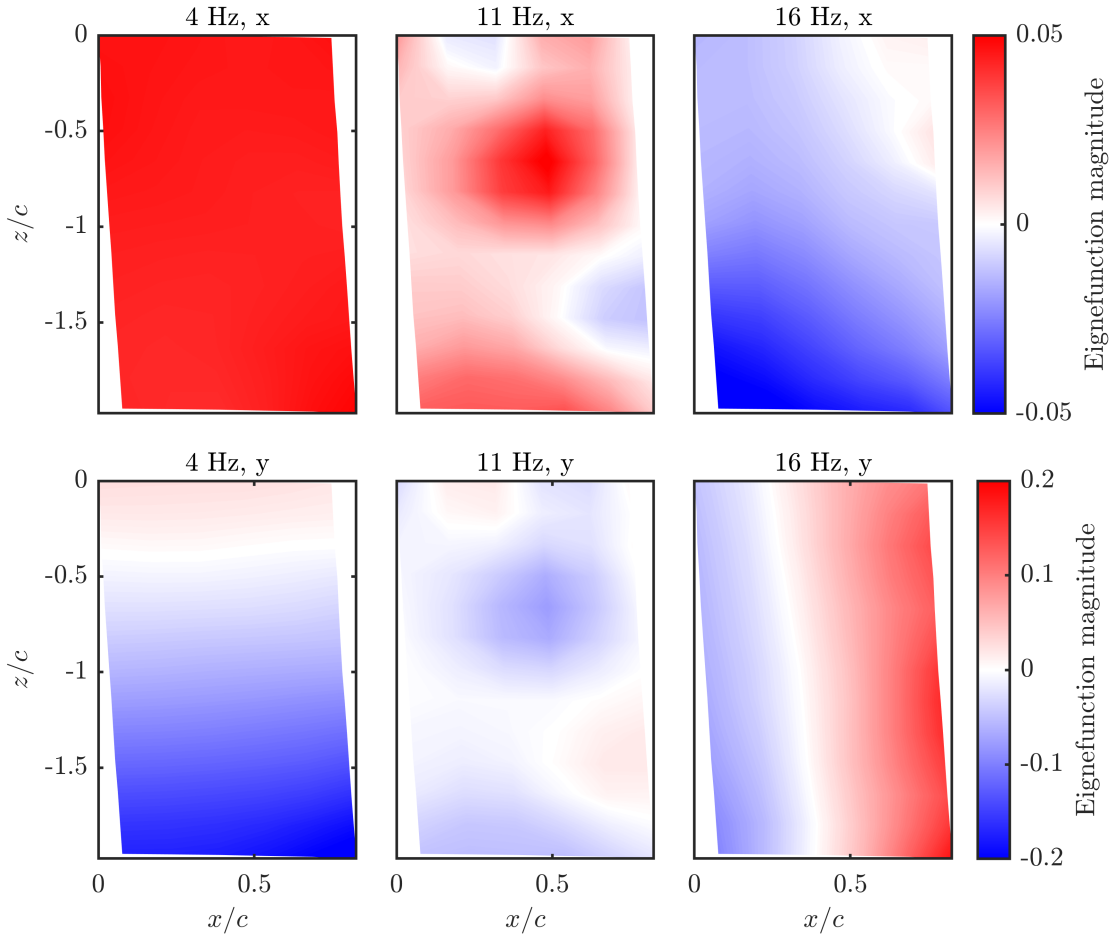

Fig. 6 Reconstructed mode shapes for the streamwise (x) and cross-stream (y) direction at 4 Hz, 11 Hz and 16 Hz. $\alpha = 18$ **degrees,** $Re = 5 \cdot 10^5$**.**

to understand what is occurring at 11 Hz.

To assess the structural response at 11 Hz, a simplified analysis method is employed. It is assumed that at any instant the deflection is linear constrains the torsional shape. To achieve this, a linear surface fit is applied to the DIC data in the form

$$b_1 z + t_1 x + t_2 xz + C = y, \tag{4}$$

where b_1 is a bending coefficient, t_1 and t_2 are torsional coefficients and C is a constant.

Spectral analysis is conducted using Welch's power spectral density estimate [25] where the DIC data are divided into blocks containing 546 snapshots with 50 % overlap. Figure 7 shows the power spectral density of the fluctuations of the bending and torsional coefficients. The bending coefficient appears at a frequency close to 4 Hz whereas the torsional coefficients appear at a frequency close to 11 Hz.

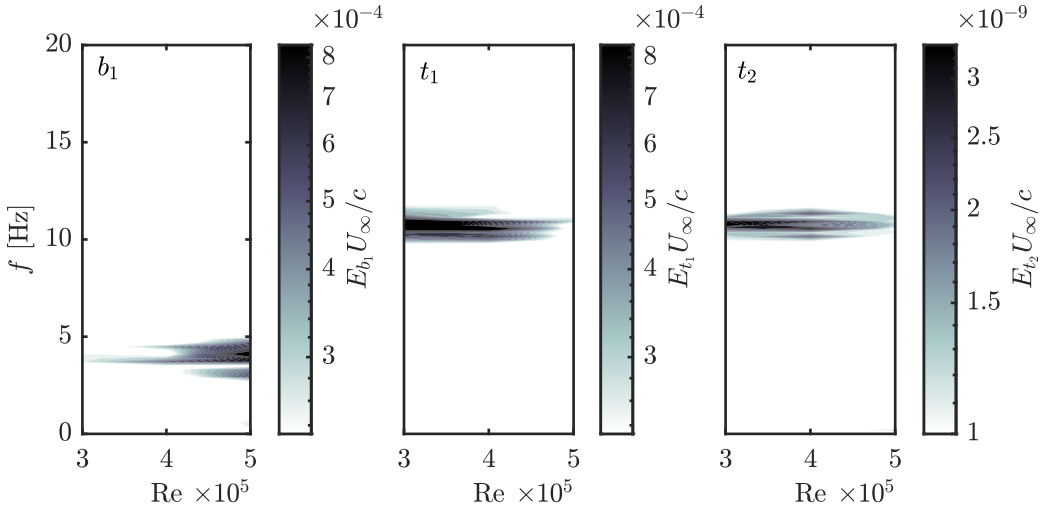

Fig. 7 Power spectral density of the (Left) b_1 coefficient, (Center) t_1 coefficient and (Right) t_2 coefficient of the linear surface fit. $\alpha = 18$ **degrees,** $Re = 3 \cdot 10^5 - 5 \cdot 10^5$**.**

A distinct spectral peak is observed at 16 Hz. Similar to the peak at 4 Hz, the first mode of the peak has an energy content one order of magnitude larger than that of the subsequent mode, so it is representative of the structural displacement. Figure 6 shows the first mode shape at 16 Hz for the streamwise (x) and cross-stream (y) direction. The wing is rotating about the cross-stream axis from a focal point at the root of the wing. In the cross-stream direction there is a clear line of rotation around the mounting point of the wing as a result of the angle of attack correction. These mode shapes suggest that there is a structural excitation related to the experimental set-up. This excitation manifests as a surge mode, whereby the structure holding the wing is rotating around the cross-stream axis.

From the above analysis, the aeroelastic wing system exhibits three structural modes when in a stalled configuration: a bending mode at 4 Hz, a torsional mode at 11 Hz and surging mode at 16 Hz. Literature [7, 9–11, 14] indicates

that the structural modes of an aeroelastic wing are excited by introducing harmonic flow perturbations. The question remains: can these structural modes also be excited by the introduction of statistically known free-stream turbulence? The first step in answering this question is to understand how the wing reacts to the introduction of FST.

B. Forces and moments

To understand how the aeroelastic wing reacts to FST, the forces and moments of the wing are measured. When evaluating the time-averaged forces and moments of the wing, figure 8 (a-d) shows that with a clean inflow, the aeroelastic NACA0012 wing stalls at an angle of attack of 12 degrees, characterised by a decrease in lift, increase in drag and reduction in pitching moment. Similar to previous literature, the introduction of FST causes the onset of stall to be delayed and the peak time-averaged lift (figure 8 (a)) coefficient to increase. The angle of maximum lift for the turbulent cases is observed to be at 16 degrees with a peak lift coefficient 10 % larger than that of the clean inflow case. Generally, the time-averaged forces and moments of the wing subjected to FST are similar. The time-averaged drag (figure 8 (b)) of the turbulent cases increases smoothly when compared to the clean inflow case as a result of the less dramatic stall. Similarly, the time-averaged pitching moment (figure 8 (c)) of the turbulent case decreases more gradually when compared to the clean inflow case. The time-averaged bending moment (figure 8 (d)) is similar for all the FST cases, with a larger moment in post stall angles (past 12 degrees) when compared to the clean inflow case.

When observing the fluctuations of the forces and moments of the wing, figure 8 (e-h) shows that the standard deviation of the clean flow measurements increases as stall occurs, and then decreases as the wing begins to act as a bluff body. With the introduction of FST, the standard deviations of the measurements increase as a result of the fluctuating inflow. In the pre-stall angles, both the smallest and largest integral length scale cases lead to an increase in fluctuations of lift (figure 8 (e)). As the wing approaches the onset of stall, the $L_x/c \approx 0.5$ case exhibits a small increase in lift fluctuations, unlike the more pronounced response observed in the other two turbulent cases. Consequently, this results in an overall increase in fluctuations of lift for the $L_x/c \approx 1.0$ case. For all angles of attack, the $L_x/c \approx 0.5$ case demonstrates a fluctuating drag (figure 8 (f)) response 35 % greater than that of the other two turbulent cases in pre-stall conditions. At pre-stall angles of attack, all three turbulent cases exhibit similar pitching moment fluctuations (figure 8 (g)), which increase most dramatically for the $L_x/c \approx 1.0$ case as the wing approaches stalled conditions. For all angles of attack, the $L_x/c \approx 1.0$ case exhibits a fluctuating bending moment (figure 8 (h)) 40 % greater than that of the other two turbulent cases. The drastic increase in fluctuating drag and bending moment for the $L_x/c \approx 0.5$ and $L_x/c \approx 1.0$ cases, respectively, suggests a unique sensitivity of the aeroelastic wing to integral length scale. The increase in fluctuating drag implies a potential aerodynamic effect triggered by an integral length scale of $L_x/c \approx 0.5$, while the increase in fluctuating bending moment suggests a possible structural excitation at an integral length scale of $L_x/c \approx 1.0$. However, to better understand these fluctuations, their frequency content must be explored.

Spectral analysis is conducted to better understand the distribution of force and moment fluctuations resulting from

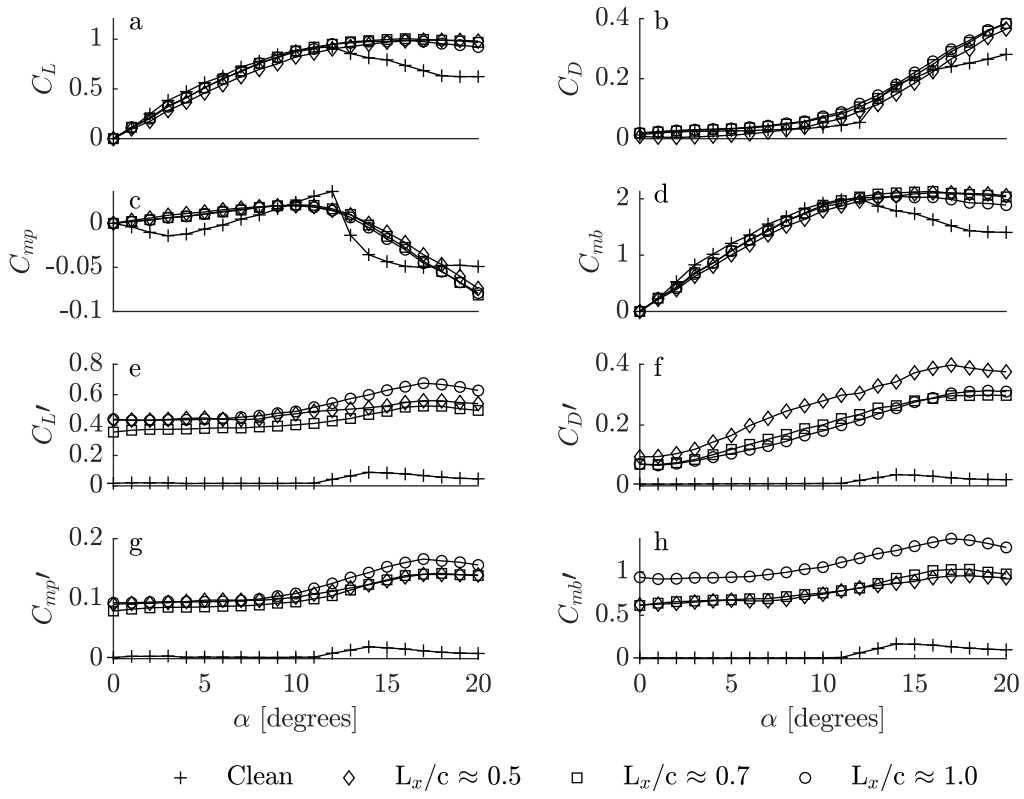

Fig. 8 (a-d) Time-averaged mean and (e-h) standard deviation of the lift, drag, bending and pitching moment coefficient against angle of attack. $\alpha = 0 - 20$ **degrees,** $Re = 2 \cdot 10^5$**.**

different integral length scales. Figure 9 displays the normalised power spectral density of the lift and drag coefficients. For the clean case, two spectral peaks are observed in the lift at 4 Hz and 22 Hz. Similarly, there is a 4 Hz and 22 Hz peak in the spectral content of the drag coefficient, in addition to a large peak at 16 Hz. There is an observed increase in power with the addition of FST by two orders of magnitude, resulting from the higher energy within the flow. There is also the introduction of spectral content over all angles of attack for the lift and drag, with a greater magnitude observed at angles larger than 15 degrees. There are no new frequencies occurring as a result of the FST, just the amplification of specific frequencies observed in the clean flow case.

As the integral length scale increases, the amplitude of the spectral content of the lift and drag appears to shift from a higher frequency to a lower frequency. For the spectral content of the lift coefficient the amplitude of the 22 Hz peak decreases by 45 % as integral length scale increases from $L_x/c \approx 0.5$ to $L_x/c \approx 1.0$, whereas the 4 Hz peak increases by 255 %. Similarly, for the drag coefficient, the 16 Hz peak decreases by 70 % with increasing integral length scale, while the 4 Hz peak increases by 235 %. Even though the integral length scale does not introduce new frequencies in the response of the aeroelastic wing, it does lead to the preferential amplification of certain frequencies over others. The 4 Hz peak observed in both lift and drag can be attributed to the structural bending mode of the wing. Therefore, it can be

concluded that with an increase in integral length scale, the structural bending mode of the aeroelastic wing is excited. Moreover, the amplitude of the 16 Hz peak in the drag coefficient can be attributed to the structural surging mode of the system and appears to be excited by a decrease in integral length scale. What is unclear is if an excitation in the bending mode is suppressing the surging mode or an excitation in the surging mode is suppressing the bending mode.

Figure 10 shows the phase averaged lift coefficient $C_L/C_{L_{max}}$ and torsional coefficient $t_1/t_{1_{max}}$ from equation 4. The phase-average is determined using the Hilbert transform. The in-phase double peak in lift and single peak in t_1 indicates that the 22 Hz peak in lift is linked to the 11 Hz structural torsion mode of the wing. Therefore, with decreasing integral length scale the torsional mode of the wing is excited. Similarly to the drag coefficient, it is unclear if an excitation in the bending mode is suppressing the torsional excitation or if the torsional excitation is suppressing the bending mode.

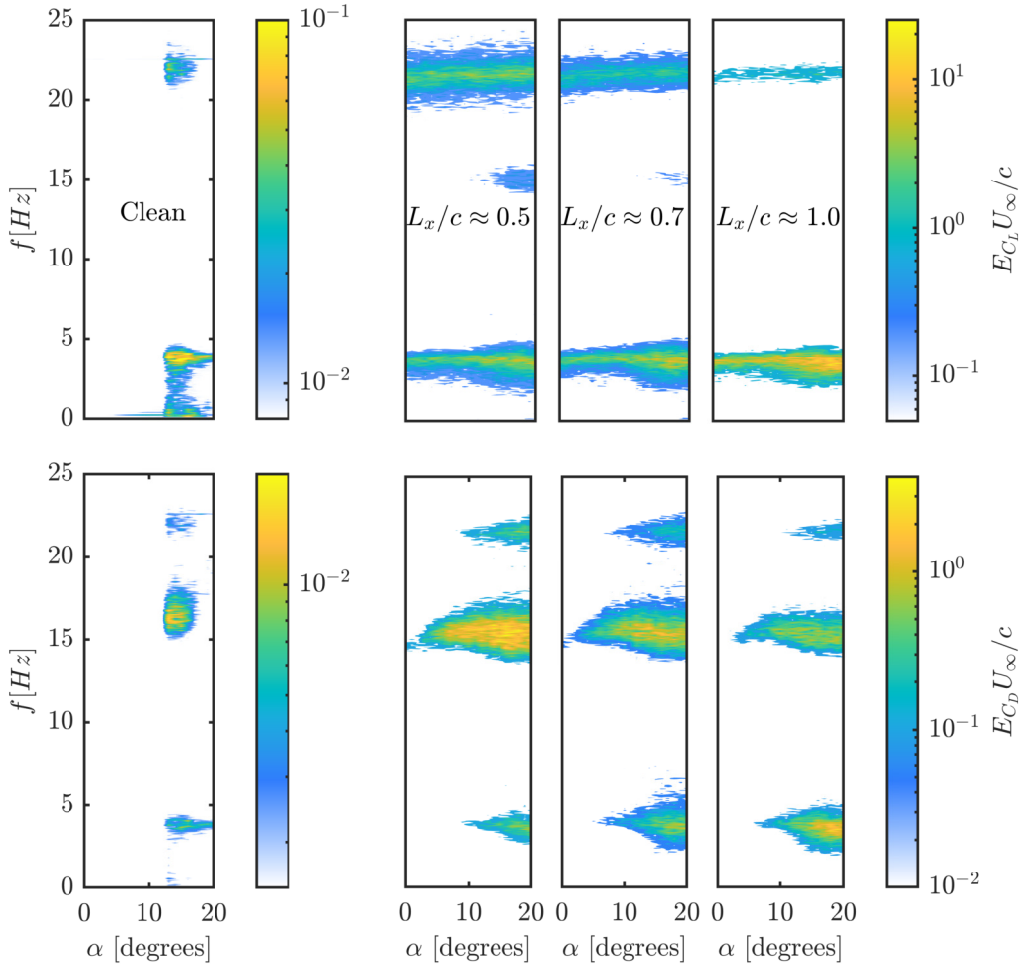

Fig. 9 Power spectral density of the measured (Top) lift and (Bottom) drag for angle of attack against frequency. $\alpha = 0 - 20$ degrees, $Re = 2 \cdot 10^5$.

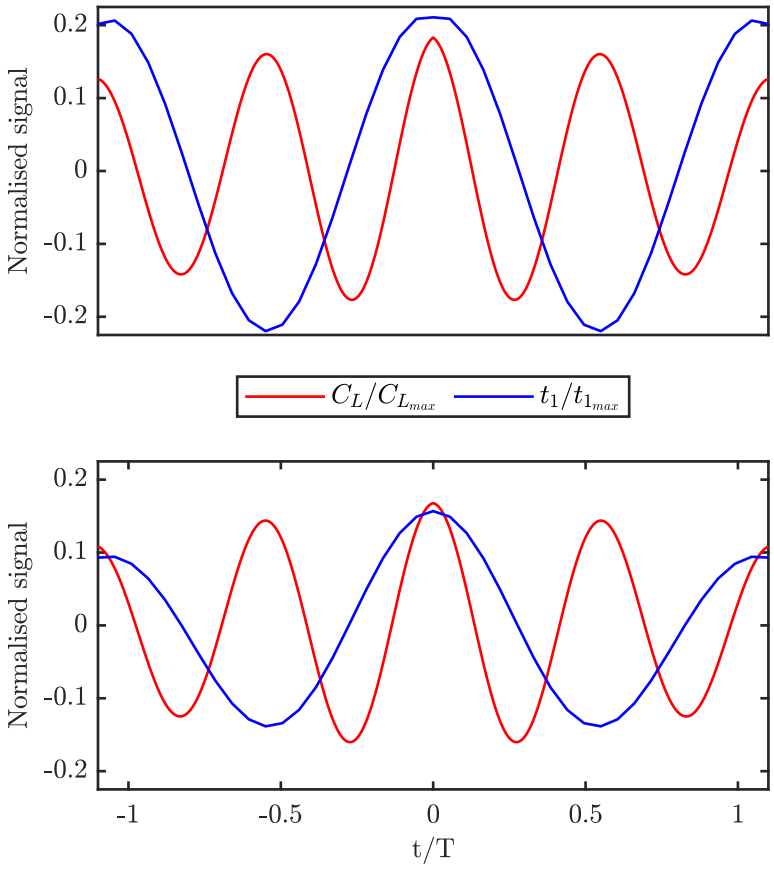

Fig. 10 Phase-averaged lift coefficient $C_L/C_{L_{max}}$ and torsional coefficient $t_1/t_{1_{max}}$. (Top) $\alpha = 18$ degrees, $Re = 3 \cdot 10^5$ and (Bottom) $\alpha = 18$ degrees, $Re = 5 \cdot 10^5$.

C. Particle image velocimetry

From the previous section, the aeroelastic wings response to FST is a delay in stall and increase in the time-averaged lift coefficient. The introduction of FST leads to the preferential amplification of certain frequencies in both the structural response and the aerodynamic forces. With increasing integral length scale a structural bending mode reduces in amplitude, whereas both a torsional and surging mode increase in amplitude. To better understand the relationship between these structural excitations and the aerodynamics of the flow field surrounding the wing, the velocity fields are investigated.

The turbulent flow fields surrounding the aeroelastic wing are measured using planar PIV to understand the excitation in structural modes with varying integral length scale. Figure 11 shows the streamwise component of the mean velocity field (filled contours) and turbulence intensity (contour lines) for each inflow case. PIV is conducted at an angle of attack of $\alpha = 16°$ as this is not only the maximum lift angle of the turbulent cases but also the angle of attack at which the largest fluctuations in the force and moments are present. The mean velocity field of the clean inflow case displays a

fully separated flow with separation occurring at the leading edge. A recirculation region is present as indicated by the blue contours which denote reversed flow. The introduction of FST appears to suppress the recirculation region, allowing the flow to remain more attached to the wing, hence the larger lift coefficient and delayed stall. No mean flow reversal is observed for any FST cases. However, due to the displacement of the wing, the velocity close to the wing's surface is not resolved which could mask a small recirculation region.

The mean velocity fields of the three turbulent cases are very similar, as expected from the similarity in time-averaged force and moment coefficients, with a slight discrepancy in the size of the wake. For the $L_x/c \approx 0.5$ case the wake region is the smallest of the turbulent cases and the flow appears most attached. For the turbulent case of $L_x/c \approx 0.7$, the wake is longer and slightly wider than that of the $L_x/c \approx 0.5$ case. For the $L_x/c \approx 1.0$ case, the wake region is again slightly larger than that of the $L_x/c \approx 0.7$ case, as attested to by the widening contours of T_u. Aside from the slightly larger wake regions, the turbulent mean fields are otherwise very similar.

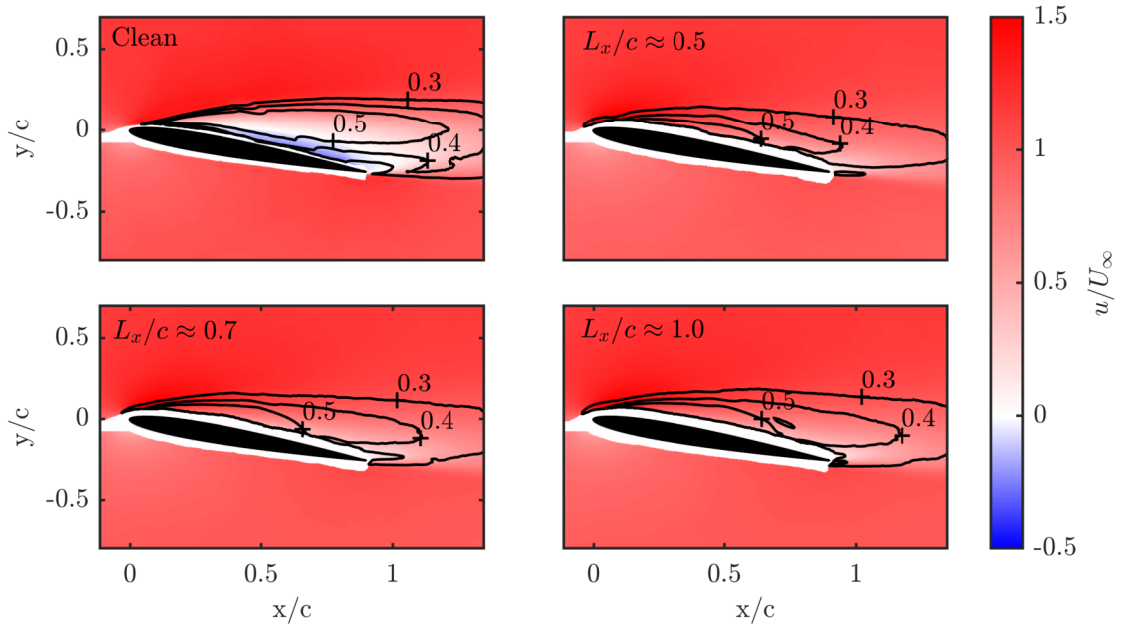

Fig. 11 Time-averaged streamwise velocity with contour lines showing T_u. $\alpha = 16$ degrees, $Re = 2 \cdot 10^5$.

The similarity of the time-averaged flow fields explains the results of the time-averaged forces, but it does not explain the differences in the fluctuations of said forces. Proper orthogonal decomposition (POD) is utilised to analyze the coherent structures within the velocity flow field. Details of the algorithm can be found in Appendix IV.A. Figure 12 shows the energy fraction of the three turbulent cases, where the energy fraction is calculated by dividing the sum of the eigenvalues from 1 to n modes by the sum of all eigenvalues. In order to recover 50 % of the energy within the flow, 5 and 9 POD modes are required for the $L_x/c \approx 0.5$ and $L_x/c \approx 1.0$ cases, respectively. The additional POD modes required for the case of $L_x/c \approx 0.5$ suggests a more complex flow field comprised of higher frequency aerodynamic

structures. These additional modes could account for the differences observed in the frequency spectra of the resulting forces on the wing.

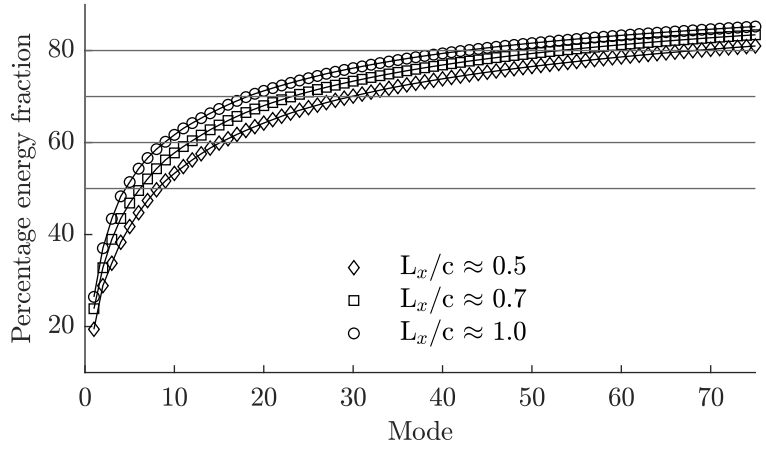

Fig. 12 Percentage energy fraction of POD modes. $\alpha = 16$ **degrees,** $Re = 2 \cdot 10^5$**.**

Figure 13 shows the absolute value of the Pearson's linear correlation coefficient for the first 20 POD mode shapes. The Pearson's linear correlation coefficient is a measure of the linear association between two variables A and B, given by

$$\rho(A, B) = \frac{1}{N-1} \sum_{i=1}^{N} \left(\frac{A_i - \mu_A}{\sigma_A} \right) \left(\frac{B_i - \mu_B}{\sigma_B} \right), \tag{5}$$

where μ and σ are the mean and standard deviation, respectively. Interestingly, there are no similarities after the initial mode for the clean and FST POD modes, indicating that the coherent structures are dissimilar. This is a significant result as the frequencies observed in the lift and drag are similar between the clean and FST cases. The POD mode-shapes of the turbulent cases are far more correlated. The correlation of the $L_x/c \approx 0.5$ and $L_x/c \approx 1.0$ cases (Figure 13, bottom left) and $L_x/c \approx 0.5$ and $L_x/c \approx 0.7$ (Figure 13, bottom middle) cases show strong similarities in the shape of the first 7 POD modes, indicating that the most energetic coherent structures of both cases are similar. After the first 7 modes there is a weaker correlation, where differences within the dynamics of the flow field around the wing are present. The $L_x/c \approx 0.7$ and $L_x/c \approx 1.0$ cases (Figure 13, bottom right) show very good agreement for nearly all 20 modes. Therefore, from this point we will only make comparisons between the $L_x/c \approx 0.5$ and $L_x/c \approx 1.0$ cases.

The introduction of the POD analysis gives insight into the coherent structures. However, due to the non-time resolved nature of the velocity fields, it does not give an understanding of how these structures propagate with time. To understand how the flow field surrounding the aeroelastic wing varies with time, multi-time delay multi-probe linear stochastic estimation (LSE) is employed. LSE uses information from the time-resolved forces and moments alongside the POD of the velocity fields to reconstruct an estimate for the time coefficients of the POD modes. The method applied in this paper is a slightly modified version of work by Durgesh and Naughton [26] described in more detail in Appendix

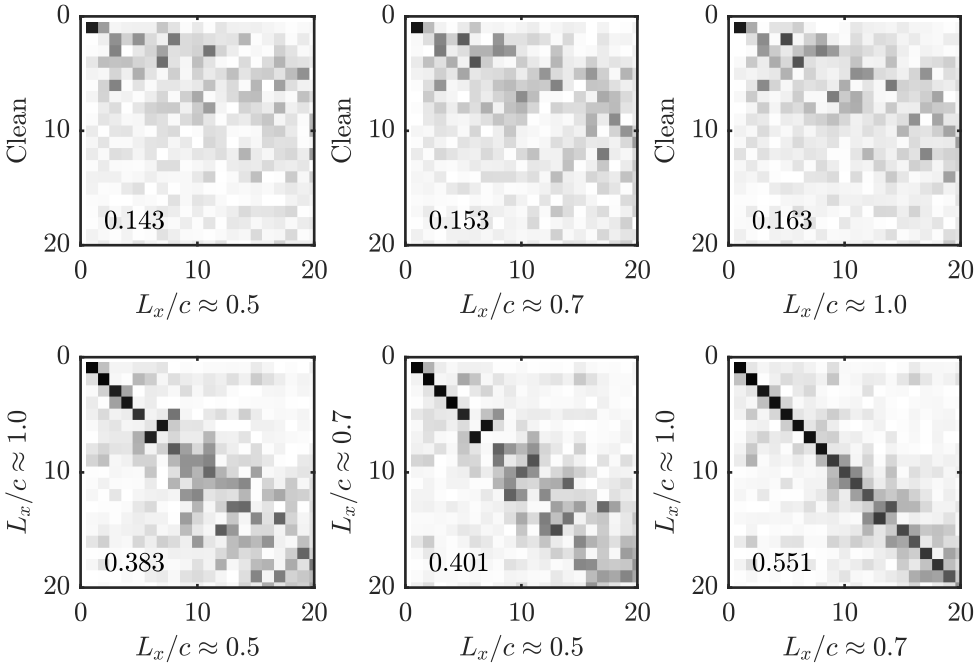

Fig. 13 Pearson's correlation coefficient of the first 20 streamwise and cross-stream velocity POD mode-shapes. The average correlation coefficient in the diagonal 2x2 is shown in each sub-plot. $\alpha = 16$ **degrees,** $Re = 2 \cdot 10^5$**.**

IV.C.

Figure 14 shows the vorticity of the reconstruction of 50 % of the energy of the LSE coefficients for the $L_x/c \approx 0.5$ and $L_x/c \approx 1.0$ cases. The flow is reconstructed at one 4 Hz and 22 Hz frequency cycle, where $1/T_4 = 4$ Hz and $1/T_{22} = 22$ Hz. The main observation of the reconstruction is that both turbulent cases exhibit different flow phenomena as a result of the interaction between the structural excitations and variations in the integral length scale of the incoming FST. The use of time-resolved PIV would provide more information about the flow physics, however LSE is still able to illustrate the differences between the interaction of aeroelastic wings with various integral length scale free-stream turbulence.

To ensure that variations in the integral length scale are driving the differences observed in both the forces and flow field, the spectral content of the FST is evaluated. Figure 3 shows that there is no distinct peak in the turbulence generation region and the spectra of the three turbulent cases are similar. The similarities in the turbulence spectra indicate that the excitation in lift and drag frequencies and differences in the surrounding flow field are solely a result of the variations in the integral length scale. To get a more complete understanding of this phenomenon, an investigation using a wing with different properties, such as increased stiffness, or by the use of a different turbulence generator, such as one with larger grid spacing, could be employed.

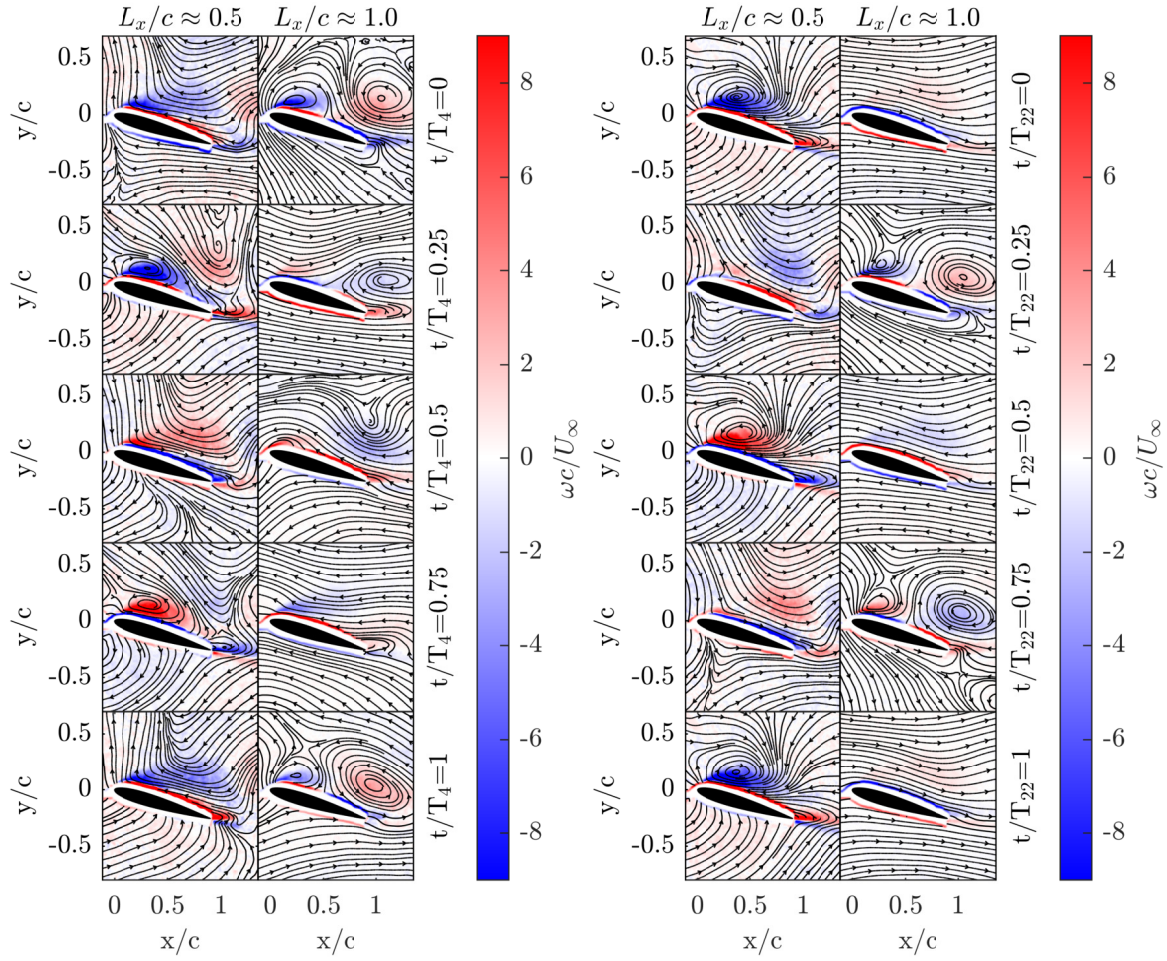

Fig. 14 Vorticity of the LSE coefficient reconstruction for one (Left) 4 Hz and (Right) 22 Hz time period. The streamlines represent the velocity fluctuations. $\alpha = 16$ **degrees,** $Re = 2 \cdot 10^5$**.**

IV. Conclusion

This study explored how the integral length scale of FST affected the stall characteristics of an aeroelastic wing at high turbulence conditions. By combining different experimental techniques, such as DIC, force and moment measurements, and PIV, the study measured the deformation, wing response, and flow fields for different integral length scales. The results showed that FST improved the time-averaged performance of the wing by delaying stall and increasing the peak lift coefficient. It was observed that the flow remained attached with the introduction of FST compared to that of clean inflow and there was a complete suppression of the recirculation bubble. However, FST also induced larger fluctuations in the forces and moments on the wing.

In the post-stall regime with a clean inflow, three frequencies (4 Hz, 16 Hz, and 22 Hz) were identified in both lift and drag measurements. These three frequencies were associated with bending, surging and torsional structural modes. Upon introducing FST, these fluctuations were amplified across a broader range of angles of attack, both pre and post-stall, without introducing new frequencies in the aeroelastic wing's response. However, varying the integral length

scale of the incoming FST led to the preferential amplification of certain frequencies over others. As the integral length scale increased from $L_x/c \approx 0.5$ to $L_x/c \approx 1.0$, the 4 Hz peak increased by over 200 %, the 16 Hz peak decreased by 70 % and the 22 Hz peak decreased by 45 %. This indicated that at higher length scales, the bending mode was excited, whereas at lower length scales, the torsional and surging modes were excited.

These structural excitations in turn influence the dynamics of the flow surrounding the wing. When analysing the POD of the velocity fields, the energy fraction was lowest for the $L_x/c \approx 0.5$ case and was largest for the $L_x/c \approx 1.0$ case. This indicated that there was a more complex flow field comprised of higher frequency aerodynamic structures for the $L_x/c \approx 0.5$ case. With the use of LSE, the POD modes were reconstructed, clearly showing different flow phenomena as a result of structural excitations from variations in integral length scale.

Appendix

A. Proper orthogonal decomposition

POD determines the modal content from a set of snapshot data, where "snapshot" denotes flowfield information captured at a specific moment in time. The resulting POD modes, orthogonal to one another, capture key features in a reduced-dimensional space. The goal of POD is to decompose $\boldsymbol{u}(x,t)$ into a set of deterministic spatial functions $\boldsymbol{\Phi}_n(x)$ multiplied by time coefficients $a_n(t)$, which is given by

$$\boldsymbol{u}(x,t) = \sum_{n=1}^{\infty} a_n(t)\boldsymbol{\Phi}_n(x), \tag{6}$$

where x is the spatial coordinate and n is the mode.

POD was first applied to fluid dynamics by Lumley [27]. Within this analysis, `MATLAB`'s `svd` function is used to generate the singular values of the snapshot matrix (where a singular value decomposition of a matrix $\boldsymbol{A}$ is such that $\boldsymbol{A} = \boldsymbol{USV}^T$) which are used to calculate the time coefficients, eigenvalues and POD mode-shapes. Due to the size of the snapshot matrix, the `svd` function is applied such that an economy-size decomposition of the snapshot matrix is determined.

B. Spectral proper orthogonal decomposition

SPOD is a frequency domain form of POD that is used to extract coherent features in data in both space and time. The goal of SPOD is to express the Fourier modes of the flow field $\hat{u}(x,\omega)$ as a linear combination of SPOD modes $\Phi_n(x,\omega)$ with expansion coefficients $\hat{a}_n(\omega)$, which is given by

$$\hat{u}(x,\omega) = \sum_{n=1}^{\infty} a_n(\omega)\Phi_n(x,\omega), \tag{7}$$

where ω is the frequency and n is the number of flow realizations. The equation shows that the flow field can be reconstructed from the SPOD modes and the expansion coefficients by taking the inverse Fourier transform. SPOD is implemented in `MATLAB` using the method described by Schmidt [28] with a Hamming window of size $N/10$, where N is the number of snapshots in each flow realization.

C. Multi-time delay multi-probe linear stochastic estimation

LSE uses information from the time-resolved forces and moments alongside the POD of the velocity fields to reconstruct an estimate for the time coefficients of the POD modes. The method applied in this paper is a slightly modified version of work by Durgesh and Naughton [26] where the LSE coefficients are evaluated in time instead of reconstructing the time coefficients. This gives an estimate of the dynamics of the time coefficients and can be interpreted as a phase-average of the time coefficients with respect to the forces at each individual velocity snapshot.

The goal is to come up with an estimate for the time coefficient $\hat{a}_n$ at a time t_k, the probability of which is given by

$$\hat{a}_n(t_k) = E\{a_n(t)|C_F(t), t_{k-m} \leq t \leq t_{k+m}\}, \tag{8}$$

where $E\{\}$ is the expected value of the event, C_F is the force coefficient and m is the time delay.

The mean square error e_n of the time coefficient of the nth POD mode is determined from the estimated and the original time coefficients, shown below

$$e_n = \langle[\hat{a}_n(t_k) - a_n(t_k)]^2\rangle, \tag{9}$$

where $\langle.\rangle$ represents the time average of the quantities.

Minimising the mean square error generates a system of linear equations for the LSE coefficients, shown below

$$\begin{bmatrix} \overline{C_{L_n}^{-m}C_{L_n}^{-m}} & \dots & \overline{C_{L_n}^{-m}C_{L_n}^{m}} & \overline{C_{L_n}^{-m}C_{D_n}^{-m}} & \dots & \overline{C_{L_n}^{-m}C_{D_n}^{m}} \\ \vdots & \ddots & \vdots & \vdots & \ddots & \vdots \\ \overline{C_{L_n}^{m}C_{L_n}^{-m}} & \dots & \overline{C_{L_n}^{m}C_{L_n}^{m}} & \overline{C_{L_n}^{m}C_{D_n}^{-m}} & \dots & \overline{C_{L_n}^{m}C_{D_n}^{m}} \\ \overline{C_{D_n}^{-m}C_{L_n}^{-m}} & \dots & \overline{C_{D_n}^{-m}C_{D_n}^{m}} & \overline{C_{D_n}^{-m}C_{L_n}^{-m}} & \dots & \overline{C_{D_n}^{-m}C_{D_n}^{m}} \\ \vdots & \ddots & \vdots & \vdots & \ddots & \vdots \\ \overline{C_{D_n}^{m}C_{L_n}^{-m}} & \dots & \overline{C_{D_n}^{m}C_{L_n}^{m}} & \overline{C_{D_n}^{m}C_{D_n}^{-m}} & \dots & \overline{C_{D_n}^{m}C_{D_n}^{m}} \end{bmatrix} \begin{bmatrix} A_{L_n}^{-m} \\ \vdots \\ A_{L_n}^{m} \\ A_{D_n}^{-m} \\ \vdots \\ A_{D_n}^{m} \end{bmatrix} = \begin{bmatrix} \overline{a_n C_{L_n}^{-m}} \\ \vdots \\ \overline{a_n C_{L_n}^{m}} \\ \overline{a_n C_{D_n}^{-m}} \\ \vdots \\ \overline{a_n C_{D_n}^{m}} \end{bmatrix}, \tag{10}$$

where C_L and C_D represent the coefficient of lift and drag, respectively, and are band pass filtered within 2 Hz and 30 Hz. A_L and A_D represent the LSE coefficients for lift and drag, respectively. These coefficients are then summed for each time shift and projected onto the POD mode-shapes to provide an indication of the time-resolved nature of the

POD modes.

Data statement

All data supporting this study will be made openly available from the University of Southampton repository upon publication.

Funding Sources

We gratefully acknowledge funding from EPSRC (Grant Ref: EP/V05614X/1) and the School of Engineering at University of Southampton for CT's PhD studentship.

Acknowledgments

The authors acknowledge the DIC data provided by Dr. R. Soares and Dr. I. Karasu.

References

[1] Cheney, J. A., Stevenson, J. P., Durston, N. E., Song, J., Usherwood, J. R., Bomphrey, R. J., and Windsor, S. P., "Bird wings act as a suspension system that rejects gusts," *Proceedings of the Royal Society B*, Vol. 287, No. 1937, 2020, p. 20201748. https://doi.org/10.1098/rspb.2020.1748.

[2] Roth, M., "Review of atmospheric turbulence over cities," *Quarterly Journal of the Royal Meteorological Society*, Vol. 126, No. 564, 2000, pp. 941–990. https://doi.org/10.1002/qj.49712656409.

[3] Shyy, W., Berg, M., and Ljungqvist, D., "Flapping and flexible wings for biological and micro air vehicles," *Progress in Aerospace Sciences*, Vol. 35, No. 5, 1999, pp. 455–505. https://doi.org/10.1016/S0376-0421(98)00016-5.

[4] Ifju, P., Jenkins, D., Ettinger, S., Lian, Y., Shyy, W., and Waszak, M., "Flexible-wing-based micro air vehicles," *40th AIAA aerospace sciences meeting & exhibit*, 2002, p. 705. https://doi.org/10.2514/6.2002-705.

[5] Gursul, I., Cleaver, D., and Wang, Z., "Control of low Reynolds number flows by means of fluid–structure interactions," *Progress in Aerospace Sciences*, Vol. 64, 2014, pp. 17–55. https://doi.org/10.1016/j.paerosci.2013.07.004.

[6] Qinfeng, G., Xi, H., Zhuo, W., and Jinjun, W., "Effects of wing flexibility on aerodynamic performance of an aircraft model," *Chinese Journal of Aeronautics*, Vol. 34, No. 9, 2021, pp. 133–142. https://doi.org/10.1016/j.cja.2021.01.012.

[7] Tang, D., and Dowell, H., "Nonlinear response of a non-rotating rotor blade to a periodic gust," *Journal of Fluids and Structures*, Vol. 10, No. 7, 1996, pp. 721–742. https://doi.org/10.1006/jfls.1996.0050.

[8] Tang, D., Cizmas, P., and Dowell, H., "Experiments and analysis for a gust generator in a wind tunnel," *Journal of Aircraft*, Vol. 33, No. 1, 1996, pp. 139–148.

[9] Tang, D., and Dowell, H., "Experimental and theoretical study of gust response for high-aspect-ratio wing," *AIAA Journal*, Vol. 40, No. 3, 2002, pp. 419–429. https://doi.org/10.2514/2.1691.

[10] Tang, D., Grasch, A., and Dowell, H., "Gust response for flexibly suspended high-aspect ratio wings," *AIAA Journal*, Vol. 48, No. 10, 2010, pp. 2430–2444.

[11] Neumann, J., and Mai, H., "Gust response: Simulation of an aeroelastic experiment by a fluid–structure interaction method," *Journal of Fluids and Structures*, Vol. 38, 2013, pp. 290–302. https://doi.org/10.1016/j.jfluidstructs.2012.12.007.

[12] Tang, D., and Dowell, H., "Experimental and theoretical study on aeroelastic response of high-aspect-ratio wings," *AIAA Journal*, Vol. 39, No. 8, 2001, pp. 1430–1441. https://doi.org/10.2514/2.1484.

[13] Dowell, E. H., *A modern course in aeroelasticity*, Vol. 264, Springer Nature, 2021.

[14] Fernandez, F., Cleaver, D., and Gursul, I., "Unsteady aerodynamics of flexible wings in transverse gusts," *Journal of Fluids and Structures*, Vol. 108, 2022, p. 103425. https://doi.org/10.1016/j.jfluidstructs.2021.103425.

[15] Fernandez, F., Cleaver, D., and Gursul, I., "Unsteady aerodynamics of a wing in a novel small-amplitude transverse gust generator," *Experiments in Fluids*, Vol. 62, No. 1, 2021, pp. 1–20. https://doi.org/10.1007/s00348-020-03100-8.

[16] Hoffmann, J., "Effects of freestream turbulence on the performance characteristics of an airfoil," *AIAA Journal*, Vol. 29, No. 9, 1991, pp. 1353–1354. https://doi.org/10.2514/3.10745.

[17] Zhang, Z., Wang, Z., and Gursul, I., "Lift enhancement of a stationary wing in a wake," *AIAA Journal*, Vol. 58, No. 11, 2020, pp. 4613–4619. https://doi.org/10.2514/1.J059872.

[18] Zhang, Z., Wang, Z., and Gursul, I., "Aerodynamics of a wing in turbulent bluff body wakes," *Journal of Fluid Mechanics*, Vol. 937, 2022, p. A37. https://doi.org/10.1017/jfm.2022.132.

[19] Zhang, Z., Wang, Z., and Gursul, I., "Effects of geometry of wings submerged in turbulent bluff-body wake," *AIAA Journal*, Vol. 61, No. 1, 2023, pp. 241–254. https://doi.org/10.2514/1.J062187.

[20] Thompson, C., Biler, H., Symon, S., and Ganapathisubramani, B., "Effects of integral length scale variations on the stall characteristics of a wing at high free-stream turbulence conditions," *Journal of Fluid Mechanics*, Vol. 974, 2023, p. A9. https://doi.org/10.1017/jfm.2023.789.

[21] Thorby, D., *Structural dynamics and vibration in practice: an engineering handbook*, Butterworth-Heinemann, 2008.

[22] Schanz, D., Gesemann, S., and Schröder, A., "Shake-The-Box: Lagrangian particle tracking at high particle image densities," *Experiments in Fluids*, Vol. 57, No. 5, 2016, pp. 1–27. https://doi.org/10.1007/s00348-016-2157-1.

[23] Istvan, M., and Yarusevych, S., "Effects of free-stream turbulence intensity on transition in a laminar separation bubble formed over an airfoil," *Experiments in Fluids*, Vol. 59, No. 3, 2018, p. 52. https://doi.org/10.1007/s00348-018-2511-6.

[24] Yarusevych, S., and Kotsonis, M., "Steady and transient response of a laminar separation bubble to controlled disturbances," *Journal of Fluid Mechanics*, Vol. 813, 2017, pp. 955–990.

[25] Welch, P., "The use of fast Fourier transform for the estimation of power spectra: a method based on time averaging over short, modified periodograms," *IEEE Transactions on Audio and Electroacoustics*, Vol. 15, No. 2, 1967, pp. 70–73. https://doi.org/10.1109/TAU.1967.1161901.

[26] Durgesh, V., and Naughton, J., "Multi-time-delay LSE-POD complementary approach applied to unsteady high-Reynolds-number near wake flow," *Experiments in Fluids*, Vol. 49, 2010, pp. 571–583. https://doi.org/10.1007/s00348-010-0821-4.

[27] Lumley, J., "The structure of inhomogeneous turbulent flows," *Atmospheric turbulence and radio wave propagation*, 1967, pp. 166–178.

[28] Schmidt, O., "Spectral proper orthogonal decomposition using multitaper estimates," *Theoretical and Computational Fluid Dynamics*, Vol. 36, No. 5, 2022, pp. 741–754. https://doi.org/10.1007/s00162-022-00626-x.